Ultralow-Power Electrically Activated Lab-on-a-Chip Plasmonic Tweezers

Ali Asghar Khorami, Mohammad Kazem Moravvej Farshi,* and Sara Darbari†
Nano Plasmo-Photonics Research Group, Faculty of ECE, Tarbiat Modares University, P.O. Box 14115-194, Tehran 1411713116, Iran

(Received 4 September 2019; revised manuscript received 23 December 2019; accepted 29 January 2020; published 26 February 2020)

We propose ultralow-power plasmonic tweezers with no external optical source. They consist of a one-dimensional array of graphene-based plasmonic units driven by the optical transitions within the underlying array of (Al, In)As/(Ga, In)As/(Al, In)As/(Ga, In)As/(Al, In)As quantum cascaded heterostructures (QCHs), electrically biased in series. Each QCH unit formed in a nanopillar can act as a built-in optical source required for exciting the localized surface plasmons (LSPs) at the surface of the overlying circular graphene nanodisk. The stimulated emission due to intersubband transition within each optical source evanesces through the top (Al, In)As cladding layer and interacts with the overlying graphene nanodisk, inducing the LSPs required for the formation of the plasmonic tweezers. Numerical simulations show, under 145–170 mV applied voltages, that the tweezers with graphene nanodisks of 16–30 nm in diameter and chemical potentials of 0.5–0.7 eV can trap polystyrene nanoparticles of 9 nm in diameter and larger, demonstrating acceptable sensitivities for variations in the nanoparticle diameter and refractive index. These lab-on-a-chip plasmonic tweezers, benefiting from their small footprints and ultralow power consumptions, which are capable of sensing and trapping nanoparticles without requiring expensive external optical sources, open up a different horizon for developing compact on-chip plasmonic tweezers.

DOI: 10.1103/PhysRevApplied.13.024072

I. INTRODUCTION

Ashkin pioneered the optical tweezers idea in the early 1970s [1] and later experimentally demonstrated their use for particle manipulation [2]. Dimensions of the particles that can be manipulated by conventional optical tweezers are diffraction-limited [3,4]. Nonetheless, exploiting the optical near field of surface-plasmon interfaces has enabled control of light beyond the diffraction limit, providing nano-optical traps [5,6]. In the 1990s and early 2000s, different groups theoretically studied nanoscopic optical tweezers [7–9]. Unlike conventional optical tweezers, plasmonic tweezers can remarkably confine the electromagnetic field at a metal-dielectric interface that is beyond the diffraction limit, with a large gradient, enhancing the trapping force. This local field enhancement in plasmonic tweezers allows the utilization of a weaker illumination, decreasing the possibility of any unintentional photothermal damage to the biological samples [10–16]. Volpe *et al.* [12] demonstrated that the surface plasmon polaritons at a water-gold interface led to a 40 times optical-force enhancement. However, a major drawback of using metal-dielectric interfaces for plasmonic trapping is the significant loss in metals and consequent heat generation that may damage the biological cells under study. Nevertheless, theoretical and experimental studies have shown that graphene, with lower resistive loss, higher thermal conductivity [17–20], and tunable plasmonic properties [21–24], can be a superior alternative for plasmonic applications. These promising properties of graphene, besides its biocompatible nature [25,26], had already led this group to design graphene-based plasmonic force switches and tweezers [27–29].

Moreover, the use of an externally biased optical-gain medium to compensate for the inherent loss of surface plasmons has led to a next generation of plasmonic devices called "spasers" [30–32]. The amplification of surface plasmons through stimulated emission, in a spaser, can generate a much stronger coherent plasmonic field than that induced by a laser source on a conventional metallic surface. The spaser characteristics depend on the geometry and material property of its resonator and gain medium, as well as how the surface plasmons are coupled out of the resonator [33–35]. Moreover, a spaser can be pumped either optically [36] or electrically [37]. An electrically pumped spaser, unlike the one pumped optically, can be a promising compact optical source for on-chip plasmonic applications [37,38].

*moravvej@modares.ac.ir
†s.darbari@modares.ac.ir

Here, we present the design of electrically pumped on-chip plasmonic tweezers, which, unlike our previously reported plasmonic tweezers [15,27–29,39,40], require no external optical pumping systems for excitation of the surface plasmons. These on-chip plasmonic tweezers, benefiting from ultralow electrical power consumption and compact miniaturized structure, are capable of trapping nanoscale particles.

II. MODEL STRUCTURE AND BASIC PHYSICS

Figure 1(a) illustrates a cross-section side view of the proposed electrically pumped plasmonic tweezers, in the x-z plane. It is composed of a one-dimensional array of interconnected graphene-based nanospasers, each resembling the one introduced by Apalkov and Stockman [32]. As shown in Fig. 1, each spaser is formed by a quantum cascade heterostructure that is composed of lattice-matched $Ga_{0.47}In_{0.53}As/Al_{0.48}In_{0.52}As/Ga_{0.47}In_{0.53}As$ nanopillars sandwiched between two nanolayers of $Al_{0.48}In_{0.52}As$. The epilayer thicknesses are designated by t_i ($i = 1$, 2, 3, 4, 5). The entire multilayered heterostructure array can be grown epitaxially on top of an In-P substrate, utilizing nanofabrication techniques similar to those explained in Refs. [41,42]. Moreover, the empty space between the nanopillars can be filled with a compatible insulating material, such as Si_3N_4, using plasma-enhanced chemical vapor deposition (PECVD) [43]. The entire array of quantum cascade heterostructures can be biased, in parallel, via the two Ti-Au ohmic contacts devised on the top and bottom interconnecting epilayers, i.e., $Al_{0.48}In_{0.52}As$ layers designated with thicknesses t_1 and t_5. Notably, these terminals are electrically isolated from the liquid within the microfluidic chamber.

As also seen in Fig. 1(a), circular graphene nanodisks of the same diameters (d) and chemical potentials (μ_C) are devised on the top $Al_{0.48}In_{0.52}As$ epilayer, so that each is cocentered with the underlying nanopillar of diameter $D > d$. For the tweezers to be accomplished, an appropriate microfluidic chamber is devised on top of the structure, as seen in Fig.1(a), through which the nanoparticles can flow above the graphene nanodisks by the fluidic drag force [44]. Figure 1(b) shows the top (x-y plane) view of the proposed on-chip plasmonic tweezers. Moreover, we assume that sufficiently dilute suspensions of nanoparticles of various diameters (green and blue) are quasi-statically entering the channel via the inlet. The sheath flows help most of the incoming nanoparticles to move very slowly above the graphene nanodisks.

Here, we briefly explain the basic physics that govern the plasmonic tweezers' functionality. When the properly designed array of spasers is electrically pumped with an appropriate external bias [Fig. 1(a)], the resulting intersubband optical transition within the top $Ga_{0.47}In_{0.53}As$ region in each spaser can originate excitation of the localized surface plasmons (LSPs) on the respective overlaying graphene nanodisk (see Appendix A). A nanoparticle positioned near the LSPs on the tip of an electrically activated spaser may experience an optical force. The gradient components of the average optical force may trap that nanoparticle above the nanodisk surface. The out-of-plane component of the gradient force can be balanced by various opposing forces, originating from thermophoresis, fluidic lift, gravity, and electrostatic mechanisms, preventing the particles from sticking to the nanodisk surface [15]. The in-plane component of the gradient force results in a gradient potential that may trap the particle. The threshold for the trapping potential energy is $-10k_BT$, wherein k_B and T are the Boltzmann constant and ambient temperature, respectively.

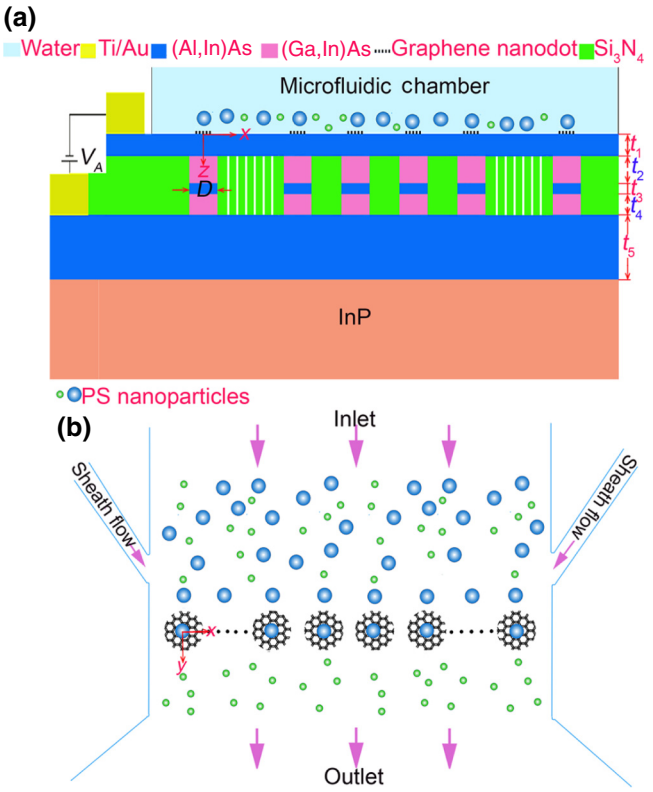

FIG. 1. (a) Side (x-z plane) view of heterostructure plasmonic tweezers devised on In-P substrate. (b) Top (x-y plane) view of the fluid chamber devised on top of tweezers containing polystyrene (PS) nanoparticles of various diameters (green and blue).

Notably, the center frequency of the intersubband optical transitions (ω_0) depends on the active region thickness, t_2, and V_A. For the LSPs to be excited on a spaser tip, the resonance frequency of the graphene nanodisk LSPs (ω_{LSPR}) should be equal to ω_0. The condition $\omega_{\mathrm{LSPR}} = \omega_0$ sets constraints on the graphene nanodisk chemical potential (μ_C) and diameter (d), as the design parameters. The

intensity of the emitted radiation in the active medium depends on the magnitude of the external electric field, which is related to the magnitude of the applied voltage and the active region diameter, D. For the spaser LSPs to be intense enough to result in the desired trapping conditions, the thickness of the top cladding layer (t_1) should be thin enough for the evanescent part of the optical field to reach the graphene nanodisk with an appropriate intensity. Above all, for a spaser to be suitable for trapping particles, it must operate in the continuous-wave (cw) regime, as discussed Secs. III and IV.

In Sec. III, we show how one can obtain the optical-plasmonic force components and the gradient potential, using the Maxwell stress tensor (MST).

III. THEORY AND SIMULATION

Using the finite-difference method to solve the coupled Schrodinger–Poisson equations self-consistently, for the given quantum cascade heterostructure [Fig. 9(a)], biased with a particular dc applied voltage, we can obtain the corresponding band structure, eigenfunctions (ψ_1 and ψ_2), and the corresponding eigenenergies (E_1 and E_2), as can be seen in Fig. 9(b). From these solutions, we can obtain the medium gain required for solving Maxwell's equations [45,46],

$$g(\mathrm{m}^{-1}) = \frac{2\omega_0\ |d_{21}|^2 n_C}{c\ \hbar\ \Gamma_{21}\ \varepsilon_0 \sqrt{\mathrm{Re}\ \varepsilon_{\mathrm{eff}}}} \tag{1}$$

where ϵ_0 and c are the permittivity and light velocity of free space, respectively; $\hbar$ is the reduced Planck constant; $\omega_0 = (E_2 - E_1)/\hbar$; and Γ_{21} is the intersubband transition rate accounting for various scatterings [47,48]. Moreover, n_C is the per volume inversion population that can be obtained from the difference between the density matrix elements ρ_{22} and ρ_{11} related to the states ψ_2 and ψ_1 [46,49]. Moreover, $d_{21} = e \int \psi_2^* z\, \psi_1 dz$ is the dipole matrix element of the intersubband transition, with e as the electron charge and Re $\varepsilon_{\mathrm{eff}}$ is the real part of the effective relative permittivity of the quantum cascade heterostructure that can be estimated by effective medium theory, i.e., $\mathrm{Re}\ \varepsilon_{\mathrm{eff}} \approx \Sigma_{i=1}^{5} t_i \big/ \Sigma_{i=1}^{5} t_i \varepsilon_i^{-1}$.

A necessary condition for cw spasing is [46]

$$g \geq \frac{\omega}{c\sqrt{\mathrm{Re}\ \varepsilon_{\mathrm{eff}}}} \frac{\mathrm{Re}\ s(\omega)}{1 - \mathrm{Re}\ s(\omega)} \mathrm{Im}\ \varepsilon_g(\omega) \equiv g_{\mathrm{th}}, \tag{2}$$

where g_{th} can be interpreted as the threshold gain needed for spasing,

$$\varepsilon_g(\omega) \approx \frac{(\varepsilon_{\mathrm{w}} + \varepsilon_{\mathrm{eff}})}{2} + i\frac{\sigma(\omega)}{\varepsilon_0 \omega\ \Delta}, \tag{3}$$

is the effective relative permittivity of the graphene, and

$$s(\omega) = \mathrm{Re}\ \varepsilon_{eff} \big/ [\mathrm{Re}\ \varepsilon_{eff} - \varepsilon_g(\omega)] \tag{4}$$

is the Bergman's spectral index [50–54] that originates from the Bergman interpretation of the observation of additional resonances found in the physical properties of macroscopically inhomogeneous media [55]. In Eq. (3), σ represents the surface optical conductivity of the graphene nanodisk, which, in the absence of an external magnetic field, can be approximated by the simplified Kubo formula, neglecting the insignificant quantum size effects on the graphene plasmons [27,56,57],

$$\begin{aligned}\sigma_g = {} & \frac{2e^2 k_B T}{\pi\hbar^2} \frac{i}{\omega_0 + i2\pi\tau_g^{-1}} \ln\left(2\cosh\frac{\mu_{\mathrm{C}}}{2k_B T}\right) \\ & + \frac{e^2}{4\hbar}\left\{\left[\frac{1}{2} + \frac{1}{\pi}\arctan\left(\frac{\hbar\omega_0 - 2\mu_{\mathrm{C}}}{2k_B T}\right)\right]\right. \\ & \left. - \frac{i}{2\pi}\ln\left[\frac{(\hbar\omega_0 + 2\mu_{\mathrm{C}})^2}{(\hbar\omega_0 - 2\mu_{\mathrm{C}})^2 + 4(k_B T)}\right]\right\},\end{aligned} \tag{5}$$

where $\tau_g = \mu_e\, \mu_C \big/ e v_F^2$ is the carrier relaxation time in graphene, with mobility $\mu_e = 10^4\ \mathrm{cm^2\ V^{-1}\ s^{-1}}$ and Fermi velocity of $v_F = 10^8\ \mathrm{cm\ s^{-1}}$. In deriving Eq. (3), we consider the graphene nanodisk to be an ultrathin dielectric layer of thickness $\Delta = 0.34$ nm that is sandwiched between an infinitely thick layer of fluid (water), with a relative permittivity of ε_W, and the quantum cascade heterostructure as an effective medium with relative permittivity of $\varepsilon_{\mathrm{eff}}$ and thickness $t \gg \Delta$. The imaginary part of the effective relative permittivity of the quantum cascade heterostructure is proportional to the medium gain, $\mathrm{Im}\ \varepsilon_{\mathrm{eff}} = -g k_0^{-1} \sqrt{\mathrm{Re}\varepsilon_{\mathrm{eff}}}$ [46,58].

Moreover, we handle the mechanism responsible for the excitation of the LSPs at the interface of the graphene with water in the fluidic chamber quasi-classically, by solving Maxwell's equations numerically.

Having obtained the field distribution at the graphene surface, using the three-dimensional finite-difference time domain (FDTD), we can now use the MST method to evaluate the average optical force exerted on the nearby nanoparticle by the corresponding LSPs [59–61],

$$\langle F \rangle = \frac{1}{2}\mathrm{Re} \oint_{\Omega} \mathbf{T}(\mathbf{r}, t) \cdot \mathbf{n}\, dS, \tag{6}$$

where

$$\begin{aligned}\mathbf{T}(\mathbf{r}, t) = {} & \varepsilon \mathbf{E}(\mathbf{r}, t) \otimes \mathbf{E}^*(\mathbf{r}, t) \\ & + \mu \mathbf{H}(\mathbf{r}, t) \otimes \mathbf{H}^*(\mathbf{r}, t) \\ & - \frac{1}{2}(\varepsilon |\mathbf{E}(\mathbf{r}, t)|^2 + \mu |\mathbf{H}(\mathbf{r}, t)|^2)\end{aligned} \tag{7}$$

is the Maxwell stress tensor; $\mathbf{r}$ and t are the position vector and time, respectively; $\mathbf{n}$ is the unit vector normal to the surface S enclosing the particle volume Ω; ε and μ are the

medium permittivity and permeability, respectively; and **E** and **H** are the electric- and magnetic-field vectors, respectively. Finally, to evaluate the trapping capability of the spaser, we obtain the distribution of the potential energy resulting from the in-plane component of the gradient force exerted on the nanoparticle in the given x-z plane [62]:

$$U(y) = -\int_{\infty}^{y} F_y(y')\,dy'. \tag{8}$$

The potential energy experienced by a dielectric particle of diameter δ and relative permittivity of ε_p that is surrounded by water, at a point in the given plane, where the light intensity is I can be simplified to [63,64]

$$U(y) = -\frac{\pi^2\delta^3}{c}\frac{(\varepsilon_p - \varepsilon_w)}{(\varepsilon_p + 2\varepsilon_w)}I. \tag{9}$$

IV. RESULTS AND DISCUSSION

First, we start with a spaser for which geometrical and physical parameters are the same as those of the spaser introduced by Apalkov and Stockman [32]. The intersubband transition and spaser characteristics, i.e., $\hbar\,\omega_0$, d_{12}, n_C, τ_{21}, g, and $\hbar\omega_{\mathrm{LSPR}} = \hbar\omega_0$, for this particular sample (S1) obtained from the numerical method discussed in Sec. III can be seen in Table I. The input parameters t_2, d, and μ_C used in this simulation are also given in the same table. Nonetheless, the geometrical and physical parameters, $D = 60$ nm, $t_1 = t_5 = 5$ nm, $t_3 = 1.5$ nm, $t_4 = 6$ nm, $\varepsilon_1 = \varepsilon_3 = \varepsilon_5 = 12.44$, $\varepsilon_2 = \varepsilon_4 = 13.9$, and $\Delta = 0.34$ nm, that are in common with other spaser samples (S2–S6) and will be discussed later in this section are also used as the input parameters.

Next, we investigate the effects of the graphene nanodisk diameter and top (Al, In)As thickness on $\hbar\omega_{\mathrm{LSPR}}$ and the corresponding mode intensity on its surface. Figure 2(a) illustrates the profile $\hbar\omega_{\mathrm{LSPR}}$ versus t_1 and d. As seen in this figure, unlike the nanodisk diameter, which has a great influence on the LSP's resonance energy, the role of the thickness of the top (Al, In)As layer in determining $\hbar\omega_{\mathrm{LSPR}}$ is insignificant. In fact, when t_1 increases from 2 to 9 nm, the Re ($\varepsilon_{\mathrm{eff}}$) increases from 13.1 to 13.32 (i.e., ∼1.6%). As a result, the variation of the plasmon energy ($\hbar\omega_{\mathrm{LSPR}}$) is less than 1%, because $\hbar\omega_{\mathrm{LSPR}} \propto d^{-1/2}(\varepsilon_w + \varepsilon_{\mathrm{eff}})^{-1/2}$ [65]. Figure 2(b) illustrates the LSP's mode intensity at the water-graphene interface normalized to that within the top (Ga, In)As region of the spaser. As expected, this figure shows that the mode intensity, for a given d, decreases with an increase in t_1. Because the top (Al, In)As layer acts as a cladding layer, wherein the emitted light evanesces through it before reaching the graphene nanodisk. From Fig. 2(b), we can observe that for $d \geq 16$ nm and $t_1 \leq 5$ nm the normalized LSP mode intensities are greater than 5×10^3. Our further investigations show that $t_1 = 5$ nm is thin enough for the LPS mode intensity to be sufficient for trapping the target nanoparticles passing near the nanodisk top surface.

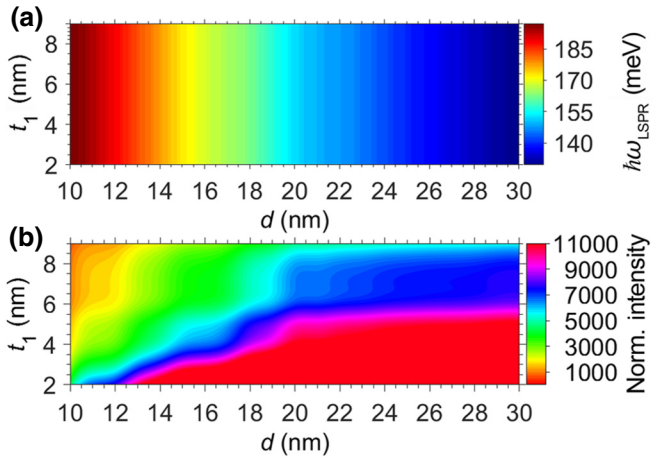

FIG. 2. Dependency of (a) $\hbar\omega_{\mathrm{LSPR}}$ and (b) corresponding normalized mode intensity on the graphene nanodisk diameter, d, and thickness of the top (Al, In)As layer, t_1, when other parameters are kept the same as those for S1 (Table I).

Then, we vary μ_C, keeping all other parameters fixed, as for the spaser S1, and evaluate the influence of μ_C on $\hbar\omega_{\mathrm{LSPR}}$ and the corresponding mode intensity at the water-graphene nanodisk interface. Figure 3(a) illustrates the simulated profile. As seen from this figure, the larger the μ_C, the larger $\hbar\omega_{\mathrm{LSPR}}$, and the greater the normalized mode intensity. In other words, as μ_C increases, the density of free electrons, and hence, the number of plasmons at

TABLE I. Simulation input parameters and resulting spaser characteristics for samples S1–S6, with common parameters of $D = 60$ nm, $t_1 = t_5 = 5$ nm, $t_3 = 1.5$ nm, $t_4 = 6$ nm, $\varepsilon_1 = \varepsilon_3 = \varepsilon_5 = 12.44$, $\varepsilon_2 = \varepsilon_4 = 13.9$, and $\Delta = 0.34$ nm.

Spaser	d (nm)	μ_C (meV)	t_2 (nm)	V_A (mV)	λ_0 (μm)	$\hbar\omega_{\mathrm{LSPR}}$ (meV)	d_{21} (e nm)	n_C ($\mu\mathrm{m}^{-3}$)	τ_{21} (ps)	g_{th} ($\mu\mathrm{m}^{-1}$)	g ($\mu\mathrm{m}^{-1}$)
S1	16	600	8.3	154.8	7.349	168.93	8.5	3.37×10^4	1.2	2.1	38
S2	30		10	154	9.569	129.75	8.75	3.75×10^4	0.95	2.07	27
S3	16	700	7.7	100.8	6.784	183	8.41	3.1×10^4	1.3	1.79	40.3
S4	30		9.6	162.6	8.947	138.77	8.78	3.66×10^4	1.1	1.77	32.7
S5	16	500	8.8	144.7	7.925	156.65	8.64	3.56×10^4	0.8	2.55	25.6
S6	30		10.7	169.2	10.318	120.33	8.9	3.68×10^4	0.9	2.49	23.5

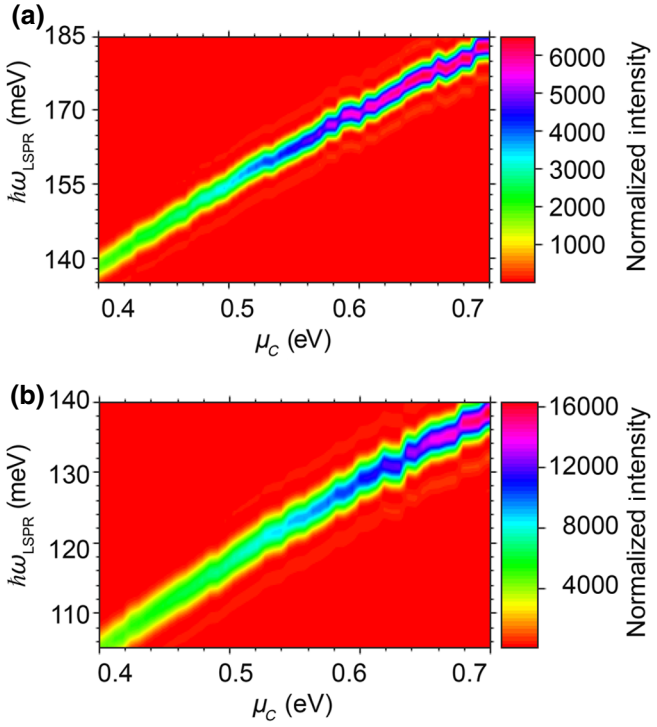

FIG. 3. Normalized mode intensity profile versus $\hbar\omega_{\mathrm{LSPR}}$ and μ_C for graphene nanodisks of diameters (a) $d = 16$ nm and (b) $d = 30$ nm.

the graphene surface increases, enhancing the plasmonic intensity. Moreover, the LSPR frequency increases with the square root of the chemical potential ($\omega_{\mathrm{LSPR}} \propto \mu_C^{1/2}$) [65].

Revisiting Fig. 2(b), we can observe that for $t_1 = 5$ and 20 nm $\leq d \leq 30$ nm the LSP's mode intensity is almost invariant. For the sake of comparison, we consider another spaser sample (S2) with $d = 30$ nm and calculate the dependencies of the normalized LSPs on the surface of the corresponding graphene nanodisk on μ_C and $\hbar\omega_{\mathrm{LSPR}}$ [see Fig. 3(b)]. The profile that is shown in Fig. 3(b) behaves similarly to that shown in Fig. 3(a), but with a larger mode intensity that is in agreement with Fig. 2(b). Setting $\hbar\omega_0 = \hbar\omega_{\mathrm{LSPR}}$ at $\mu_C = 0.6$ eV from Fig. 3(b) and solving the coupled Schrodinger equation self-consistently, we obtain t_2 and V_A for spaser sample S2, as shown in Table I.

Moreover, we choose four new samples from Figs. 3(a) and 3(b): two with $\mu_C = 0.7$ eV [i.e., S3 from Fig. 3(a) and S4 from Fig. 3(b)] and two with $\mu_C = 0.5$ eV [i.e., S5 from Fig. 3(a) and S6 from Fig. 3(b)]. Then, for each case, we solve the coupled Schrodinger-Poisson equations self-consistently to find the required t_2 and V_A for achieving the intersubband transition of energy $\hbar\omega_0 = \hbar\omega_{\mathrm{LSPR}}$. The simulated spaser characteristics for samples S3–S6 are also given in Table I. A comparison of data in the last two columns of Table I clearly indicates that $g \geq g_{\mathrm{th}}$ for all six spasers, guaranteeing cw operation required for nanoparticle trapping.

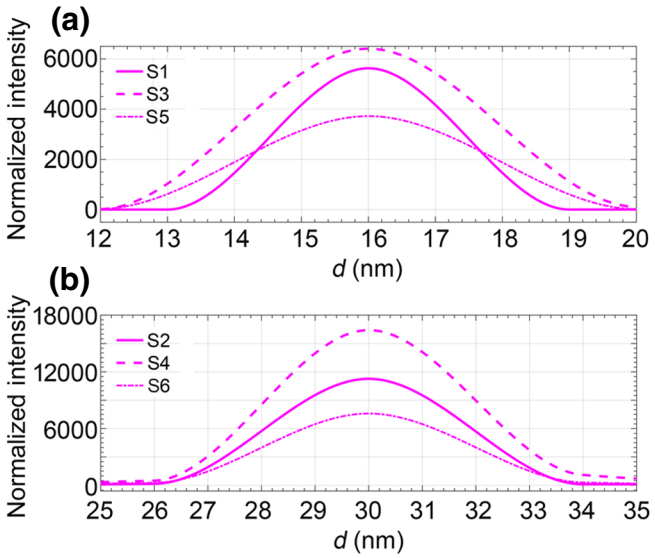

FIG. 4. Normalized mode intensity profile versus d at the top surface of the graphene nanodisk of samples (a) S1, S3, and S5; and (b) S2, S4, and S6, with parameters given in Table I.

Now, to make sure that the parameters related to the samples with $d = 16$ and 30 nm, given in Table I for each sample, correspond to the peak LSP mode intensity at resonance frequency in that sample, we vary d about the given value for each case and calculate the normalized LSP mode intensity on the given nanodisk top surface. Figure 4(a) shows that the mode intensities for S1, S3, and S5 are all optimized for $d = 16$ nm, and Fig. 4(b) similarly shows that the mode intensities for S2, S4, and S6 are optimized for $d = 30$ nm.

Having obtained the optimized design parameters, for each of the six proposed spaser samples (S1–S6) given in Table I, we are prepared to evaluate their trapping capabilities. Other research groups [66,67] have experimentally demonstrated that the plasmonic tweezers can trap nanoparticles when they are within the plasmonic active nano space, i.e., about 10–15 nm above the plasmonic surface. Figure 5 illustrates the profiles of normalized mode intensities calculated in the x-y plane positioned at 12 nm above the graphene nanodisks of samples S1–S6, as an example. For details of the field penetration in water above the nanodisk for each sample, see Appendix B.

Now, considering spherical PS nanoparticles of diameter $\delta = 14$ nm, we use Eqs. (6)–(8) to calculate the components of the average plasmonic force exerted on the nanoparticle and the resulting gradient potential experienced by it along the y direction in the aforementioned x-z plane. The dotted, dotted-dashed, and dashed lines in Figs. 6(a)–6(f) (left axes) represent the x, y, and z components, respectively, of the average plasmonic force exerted on the given particles by spaser samples S1–S6. The solid lines in the same figures (right axes) represent the resultant gradient potentials that the particles experience. As can be seen

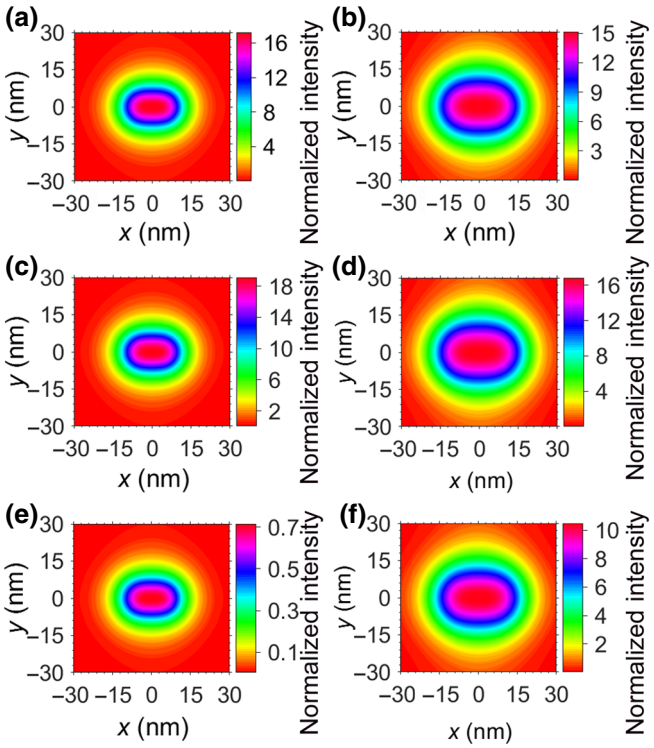

FIG. 5. Normalized LSP mode intensity in x-y plane 12 nm above the graphene nanodisk surface of (a) S1, (b) S2, (c) S3, (d) S4, (e) S5, and (f) S6.

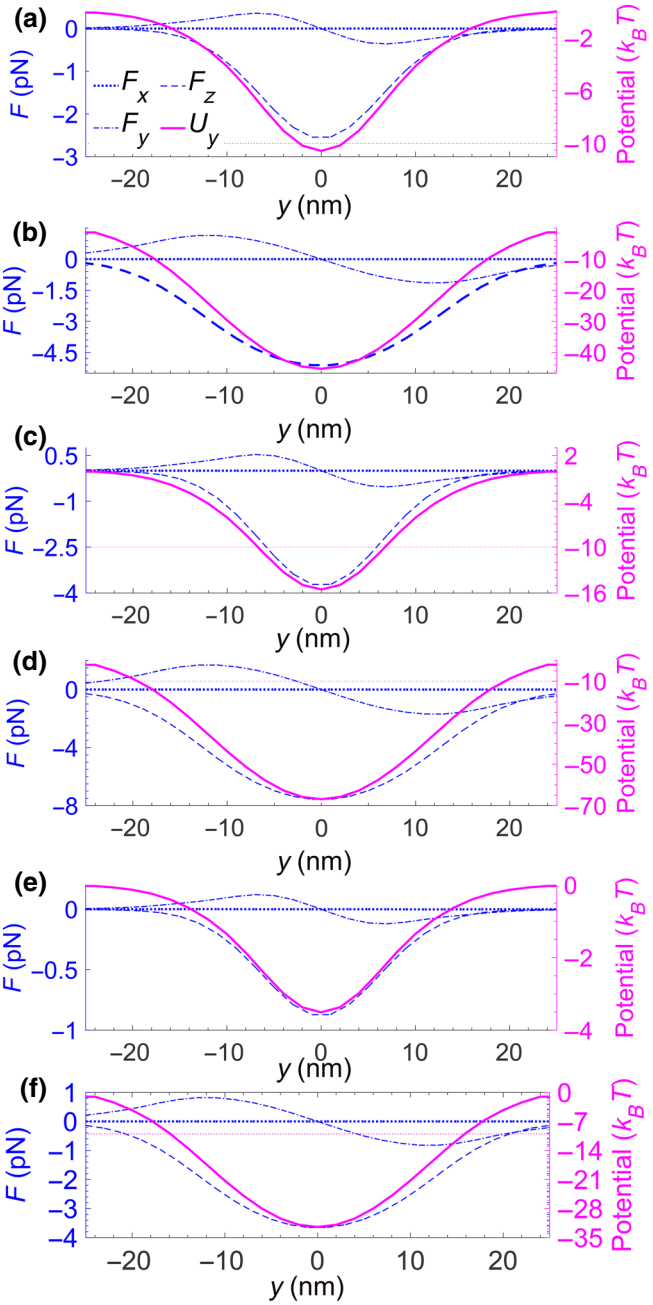

FIG. 6. Components of plasmonic force (left axis) exerted on a PS nanoparticle of diameter $\delta = 14$ nm traveling along the y direction of the x-y plane at $z = -12$ nm, and the resulting potential (right axis) in (a) S1, (b) S2, (c) S3, (d) S4, (e) S5, and (f) S6. Dotted, dotted-dashed, and dashed lines represent components F_x, F_y, and F_z, respectively.

from the dotted lines in Figs. 6(a)–6(f), the scattering component of the plasmonic force exerted on the nanoparticle is negligible, i.e., $F_x \approx 0$. Nonetheless, the dashed lines in each case show that the out-of-plane component of the gradient force (F_z) is negative, attracting the nanoparticle toward the graphene nanodisk surface. However, this component can be balanced by various opposing forces, originating from the thermophoresis, fluidic lift, gravity, and electrostatic mechanisms, preventing the particle from sticking to the surface [15]. The dotted-dashed lines, in each case, demonstrate that the in-plane component of the gradient force changes its sign at the center of the nanodisk ($y = 0$). Hence, as shown by the solid lines in each case in Figs. 6(a)–6(f), the depth of the corresponding potential well along the y direction [Eq. (7)] occurs at $y = 0$. As observed from Figs. 6(a)–6(d) and Fig. 6(f), over a particular range of y, in each of the five cases, $U_y \leq -10\ k_BT$, i.e., the potential depths induced by the LSPs of S1–S4 and S6 on the corresponding nanoparticle are sufficiently deep enough to overcome the Brownian motion of the trapped particle. The 10 k_BT potential depth is the threshold for overcoming any excess energy that the trapped particle may gain upon stochastic interaction with energetic molecules in the surrounding medium [68]. In other words, this is a precondition set to guarantee stable trapping. However, as observed from Fig. 6(e), $|U_y(y)| < 10\ k_BT$ over the entire surface of spaser S5. In other words, the potential energy created by the S5 LSPs is not deep enough to efficiently trap the PS nanoparticle of diameter $\delta = 14$ nm.

Nonetheless, our further investigations show that for S5 to trap a PS nanoparticle efficiently, the particle radius should be $\delta \geq 16$ nm (open circles in Fig. 7). Moreover, simulations also show that S6 can efficiently trap PS nanoparticles of $\delta \geq 9$ nm (solid circles in Fig. 7).

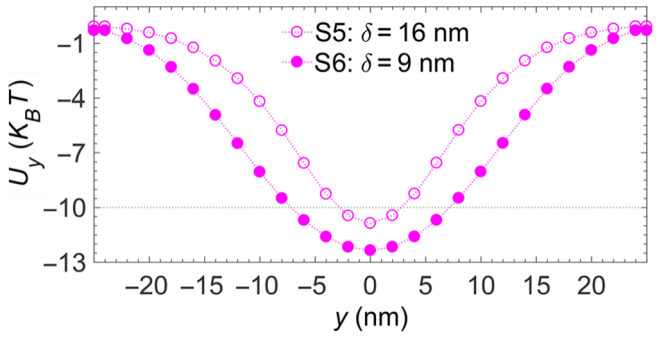

FIG. 7. $U_y(y)$ sensed by a PS nanoparticle of $\delta = 16$ nm in S5 (○) and that of $\delta = 9$ nm in S6 (•).

Finally, we investigate the sensitivities of samples S1 and S2 to minute changes in the nanoparticle refractive index (n) and diameter (δ), as two examples. Solid circles in Fig. 8(a) illustrate the variation in $U_y(x = 0, y = 0, z = -12$ nm) versus the particle refractive index ($1.55 \leq n \leq 1.6$) for S1 (left axis), whereas the solid diamonds represent a similar variation for S2 (right axis). These two sets of data show that, as the particle refractive index increases slightly, the depths of these two potential energies also increase with nearly constant slopes. This behavior is in accordance with Eq. (8). Consider a minute change of η in polystyrene refractive index (i.e., $n_p = 1.55 + \eta$, where $0.01 \leq \eta \leq 0.05$) and substitute $\varepsilon_p = (1.55 + \eta)^2$ in the multiplier $(\varepsilon_p + 2\varepsilon_w)^{-1}(\varepsilon_p - \varepsilon_w)$ in Eq. (9). You will see that the ratio can be estimated by the linear relation $(0.11 + 0.47\eta)$, over the narrow range of $1.55 \leq n_p \leq 1.6$. From the linear slopes of the data presented in Fig. 8(a), we can estimate that the trapping sensitivities to a minute change in the particle refractive index are $S_n = dU/dn_p \approx -62\ k_BT$ per refractive index unit (r.i.u. for S1) and $-210\ k_BT$/r.i.u. (for S2).

Moreover, the data depicted by solid circles (diamonds) in Fig. 8(b) represent the variation of the potential energy experienced by a PS nanoparticle positioned at ($x = 0$, $y = 0, z = -12$ nm) in S1 (S2) versus its diameter. According to Eq. (9), $U \propto \delta^3$. However, applying a minute change of ξ in the nanoparticle diameter around $\delta_0 = 14$ nm (i.e., $\delta = \delta_0 + \xi$, where $\xi \leq 1$ nm), we can estimate the corresponding multiplier in Eq. (9) by $\delta^3 \approx \delta_0^2(\delta_0 + 3\xi)$ over the given narrow range. The nearly constant slopes of the data shown in Fig. 8(b) reveal that the trapping sensitivity to a minute change in the particle diameter for S1 (S2) is $S_\delta = dU/d\delta \approx -1.2$ $(-5.6)\ k_BT$/nm.

One of the advantages of the proposed tweezers, besides their built-in optical sources, lies with the large number of plasmonic units, each capable of trapping a single target nanoparticle. Presuming one or more of the spasers do not function properly, for any reason, and fail to trap the target nanoparticles, there would be many more to function.

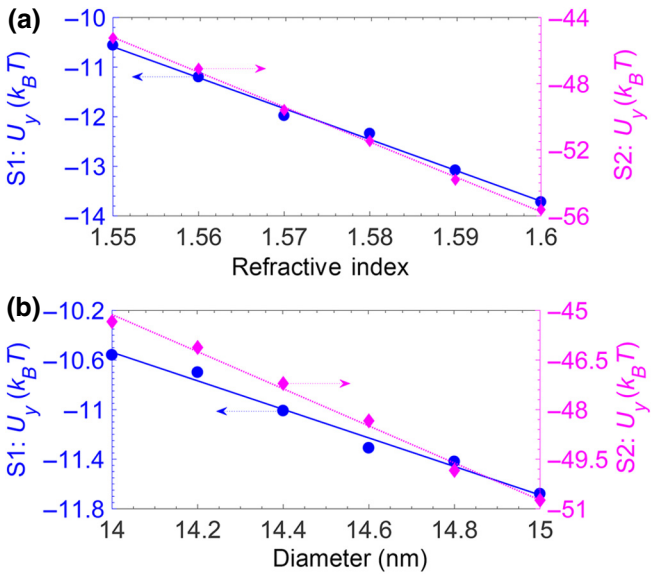

FIG. 8. Potential energy experienced by a nanoparticle at coordinates ($x = 0, y = 0, z = -12$ nm) versus its (a) refractive index (n) and (b) diameter (δ) in S1 (•: left axis) and S2 (♦: right axis).

V. CONCLUSION

We propose ultracompact lab-on-a-chip tweezers that have no need for any external optical source. Each device is composed of a number of plasmonic units that are connected in parallel and can be activated electrically with an ultralow external applied voltage ($V_A \leq 170$ mV). The entire plasmonic unit, in each system, is covered by a fluidic chamber through which the target nanoparticles can flow by a driving fluidic force and is isolated from the biasing terminals. Each plasmonic unit is made of a spaser that consists of a quantum cascade heterostructure [(Al, In)As/(Ga, In)As/(Al, In)As/(Ga, In)As/(Al, In)As/(Al, In)As] topped with a graphene nanodisk of given chemical potential (μ_C) and diameter (d). When the designed multilayer heterostructures are appropriately biased, the resulting intersubband optical emission within each active region can act as an internal optical source. This emission, evanescing through the top (Al, In)As nanolayer and interacting with the graphene nanodisk, can excite the desired LSPs on its top surface. These LSPs with adequate intensity can sense and trap nanoparticles of specific refractive indexes (n_p) and diameters (δ). In our designs, we use graphene nanodisks of diameters $d = 16$ and 30 nm, each with three different chemical potentials (i.e., $\mu_C = 0.5$, 0.6, and 0.7 eV). Our numerical investigations show that the tweezers consist of spasers with graphene nanodisk of $d = 16$ nm and $\mu_C = 0.5$, when operating under an applied voltage of $V_A = 144.7$ mV, can trap PS nanoparticles of $\delta \geq 16$ nm. Nonetheless, by solely altering the nanodisk diameters to $d = 30$ nm, the required applied voltage at which the spasers operate

appropriately is 169.2 mV, for which the tweezers can trap PS nanoparticles of diameters as small as 9 nm. We also calculate the trapping sensitivities of the tweezers to minute changes in the nanoparticles' refractive indices (S_n) and diameters (S_δ). As an example, for tweezers with $\mu_C = 0.6$ eV, $S_n \approx -62\ k_BT$/r.i.u. and $S_\delta \approx -1.2\ k_BT$/nm for $d = 16$ nm, and $S_n \approx -210\ k_BT$/r.i.u. and $S_\delta \approx -5.6\ k_BT$/nm for $d = 30$ nm.

ACKNOWLEDGMENT

This work is supported by Tarbiat Modares University through Grant No. IG-39703.

APPENDIX A: SPASER BAND DIAGRAM

Figure 9(a) illustrates a side view of spaser S1, with the same geometrical and physical parameters as those used in Ref. [32]. Using the finite-difference method, we self-consistently solve the coupled Schrodinger–Poisson equations to obtain the band diagram of the quantum cascade heterostructure underlying the top graphene nanodisk, as depicted in Fig. 9(b). The eigenfunctions ($\psi_{1,2}$) and corresponding eigenvalues ($E_{1,2}$) are depicted in the band diagram. Moreover, the coordinates of the horizontal and vertical axes reveal the epilayer thicknesses, t_i ($i = 1, 2, \ldots 5$), and the barrier heights between the adjacent quantum wells and the dc applied bias, V_A. In obtaining these solutions, we set the intersubband transition frequency, $\omega_0 = (E_2 - E_1)/\hbar$, equal to the resonant frequency of the LSPs on the graphene nanodisk, ω_{LSPR} (see Table I for S1). Notably, a crucial role of the second quantum well (i.e., the top (Al, In)As epilayer of thickness t_4), besides its role in obtaining the desired solutions, is to facilitate and speed up the process of electron extraction from the lower subband (E_1) via the bottom (Al, In)As epilayer (t_5) into the output terminal, enhancing the population inversion.

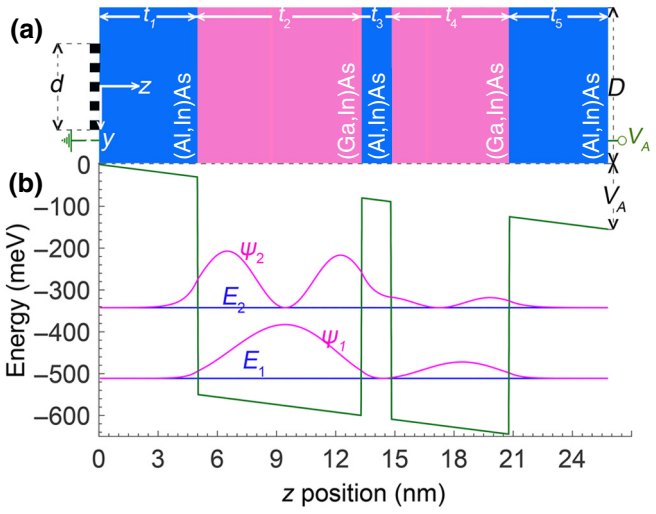

FIG. 9. (a) Cross-section view of the plasmonic unit of the proposed tweezers, (b) corresponding conduction band diagram for the operating condition shown as S1 in Table I. $E_{1(2)}$ represents the first (second) energy levels of quantum cascade heterostructure, corresponding to eigenfunction $\psi_{1(2)}$. $D = 60$ nm, $d = 16$ nm.

APPENDIX B: FIELD PENETRATION IN WATER

The LSP profiles above the graphene nanodisk surface in each sample depend on the overall dispersive properties of that particular spaser constituent at the given applied bias and liquid permittivity. Figure 10 illustrates the normalized electric-field distributions above the nanodisk surface in water (i.e., along the $-z$ direction in the x–z plane at $y = 0$) for samples S1–S6. As observed in this figure, the plasmonic field on the surface of the nanodisk in each sample maximizes near its perimeter. Furthermore, the color contours in each sample reveal that, as the field penetrates in the $-z$ direction, the corresponding maxima converge to

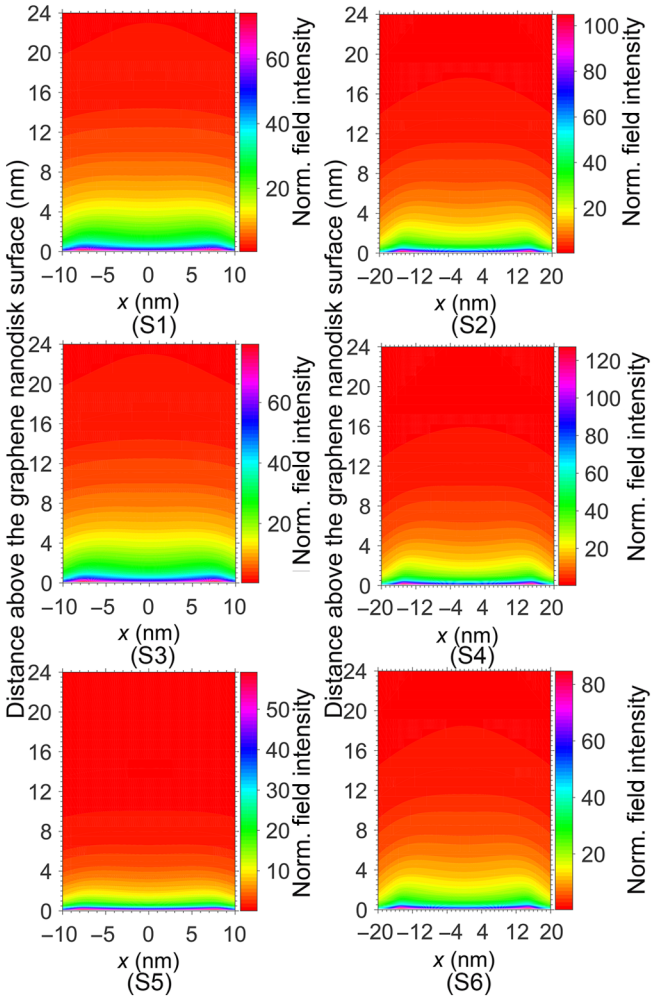

FIG. 10. Distributions of normalized field intensities above the surface of the graphene nanodisk (in $-z$ direction) in the x–z plane at $y = 0$ for each of the six samples S1–S6.

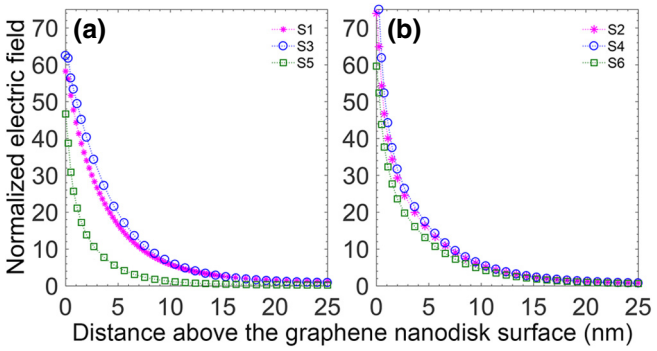

FIG. 11. Penetration of the field in water above the center of each nanodisk in samples (a) S1, S3, and S5; and (b) S2, S4, and S6.

form a monopole in a focal plane about 10.42 nm above the 16 nm nanodisks (i.e., S1, S3, and S5) and nearly 11.39 nm above the 30 nm nanodisks (i.e., S2, S4, and S6). Figure 11 shows details of field penetration along the $-z$ direction at $x = 0$ and $y = 0$. From these data, one can see that the smallest and largest attenuation constants of nearly 0.18 and 0.25 nm^{-1}, respectively, belong to samples S1 and S5.

[1] A. Ashkin, Acceleration and Trapping of Particles by Radiation Pressure, Phys. Rev. Lett. **24**, 156 (1970).

[2] A. Ashkin, J. M. Dziedzic, J. Bjorkholm, and S. Chu, Observation of a single-beam gradient force optical trap for dielectric particles, Opt. Lett. **11**, 288 (1986).

[3] D. G. Grier, A revolution in optical manipulation, Nature. **424**, 810 (2003).

[4] K. Dholakia and P. Reece, Optical micromanipulation takes hold, Nano Today **1**, 18 (2006).

[5] E. J. s. Ozbay, Plasmonics: Merging photonics and electronics at nanoscale dimensions, Science **311**, 189 (2006).

[6] J. A. Schuller, E. S. Barnard, W. Cai, Y. C. Jun, J. S. White, and M. L. Brongersma, Plasmonics for extreme light concentration and manipulation, Nat. Mater. **9**, 193 (2010).

[7] L. Novotny, R. X. Bian, and X. S. Xie, Theory of Nanometric Optical Tweezers, Phys. Rev. Lett. **79**, 645 (1997).

[8] O. J. Martin and C. Girard, Controlling and tuning strong optical field gradients at a local probe microscope tip apex, Appl. Phys. Lett. **70**, 705 (1997).

[9] K. Okamoto and S. J. P. r. l. Kawata, Radiation Force Exerted on Subwavelength Particles Near a Nanoaperture, Phys. Rev. Lett. **83**, 4534 (1999).

[10] M. Gu, J.-B. Haumonte, Y. Micheau, J. W. Chon, and X. J. A. P. L. Gan, Laser trapping and manipulation under focused evanescent wave illumination, Appl. Phys. Lett. **84**, 4236 (2004).

[11] V. Garcés-Chávez, R. Quidant, P. Reece, G. Badenes, L. Torner, and K. Dholakia, Extended organization of colloidal microparticles by surface plasmon polariton excitation, Phys. Rev. B. **73**, 085417 (2006).

[12] G. Volpe, R. Quidant, G. Badenes, and D. Petrov, Surface Plasmon Radiation Forces, Phys. Rev. Lett. **96**, 238101 (2006).

[13] M. L. Juan, M. Righini, and R. Quidant, Plasmon nano-optical tweezers, Nature Photonics. **5**, 349 (2011).

[14] A. Cuche, A. Canaguier-Durand, E. Devaux, J. Hutchison, C. Genet, and T. J. Ebbesen, Sorting nanoparticles with intertwined plasmonic and thermo-hydrodynamical forces, Nano Lett. **13**, 4230 (2013).

[15] M. Ghorbanzadeh, M. K. Moravvej-Farshi, and S. Darbari, Designing a plasmonic optophoresis system for trapping and simultaneous sorting/counting of micro-and nanoparticles, J. Lightwave Technol. **33**, 3453 (2015).

[16] Z. Chen, F. Zhang, Q. Zhang, J. Ren, H. Hao, X. Duan, P. Zhang, T. Zhang, Y. Gu, and Q. Gong, Blue-detuned optical atom trapping in a compact plasmonic structure, Photonics Res. **5**, 436 (2017).

[17] A. Vakil and N. J. S. Engheta, Transformation optics using graphene, Science **332**, 1291 (2011).

[18] E. Hwang and S. D. Sarma, Dielectric function, screening, and plasmons in two-dimensional graphene, Phys. Rev. B. **75**, 205418 (2007).

[19] J. Chen, M. Badioli, P. Alonso Gonzalez, S. Thongrattanasiri, F. Huth, J. Osmond, M. Spasenovic, A. Centeno, A. Pesquera, and P. Godignon, Optical nano-imaging of gate-tunable graphene plasmons, Nature **487**, 77 (2012).

[20] L. Ju, B. Geng, J. Horng, C. Girit, M. Martin, Z. Hao, H. A. Bechtel, X. Liang, A. Zettl, and Y. R. Shen, Graphene plasmonics for tunable terahertz metamaterials, Nature Nanotechnol. **6**, 630 (2011).

[21] A. A. Balandin, S. Ghosh, W. Bao, I. Calizo, D. Teweldebrhan, F. Miao, and C. N. Lau, Superior thermal conductivity of single-layer graphene, Nano Lett. **8**, 902 (2008).

[22] J.-D. Kim and Y. G. Lee, Graphene-based plasmonic tweezers, Carbon **103**, 281 (2016).

[23] J. Zhang, W. Liu, Z. Zhu, X. Yuan, and S. Qin, Towards nano-optical tweezers with graphene plasmons: Numerical investigation of trapping 10-nm particles with mid-infrared light, Sci. Rep. **6**, 38086 (2016).

[24] L. Wang, M. Bie, W. Cai, X. Zhang, and J. Xu, Graphene Plasmonic Tamm States with Ultracompact Footprint, Phys. Rev. Appl. **12**, 024057 (2019).

[25] M. Jablan, H. Buljan, and M. Soljacic, Plasmonics in graphene at infrared frequencies, Phys. Rev. B **80**, 245435 (2009).

[26] F. H. Koppens, D. E. Chang, and F. J. Garcia de Abajo, Graphene plasmonics: A platform for strong light-matter interactions, Nano Lett. **11**, 3370 (2011).

[27] M. Ghorbanzadeh, S. Darbari, and M. K. Moravvej-Farshi, Graphene-based plasmonic force switch, Appl. Phys. Lett. **108**, 111105 (2016).

[28] M. Samadi, S. Darbari, and M. K. Moravvej-Farshi, Numerical investigation of tunable plasmonic tweezers based on graphene stripes, Sci. Rep. **7**, 14533 (2017).

[29] M. M. Abbasi, S. Darbari, and M. K. Moravvej-Farshi, Tunable plasmonic force switch based on graphene nano-ring resonator for nanomanipulation, Opt. Express **27**, 26648 (2019).

[30] D. J. Bergman and M. I. Stockman, Surface Plasmon Amplification by Stimulated Emission of Radiation: Quantum Generation of Coherent Surface Plasmons in Nanosystems, Phys. Rev. Lett. **90**, 027402 (2003).

[31] M. I. Stockman, Spasers explained, Nat. Photonics. **2**, 327 (2008).

[32] V. Apalkov and M. I. Stockman, Proposed graphene nanospaser, Light Sci. Appl. **3**, e191 (2014).

[33] B. Liu, W. Zhu, S. D. Gunapala, M. I. Stockman, and M. Premaratne, Open resonator electric spaser, ACS Nano. **11**, 12573 (2017).

[34] L. Kumarapperuma, M. Premaratne, P. K. Jha, M. I. Stockman, and G. P. Agrawal, Complete characterization of the spasing (LL) curve of a three-level quantum coherence enhanced spaser for design optimization, Appl. Phys. Lett. **112**, 201108 (2018).

[35] M. Noginov, G. Zhu, A. Belgrave, R. Bakker, V. Shalaev, E. Narimanov, S. Stout, E. Herz, T. Suteewong, and U. Wiesner, Demonstration of a spaser-based nanolaser, Nature. **460**, 1110 (2009).

[36] C. Rupasinghe, I. D. Rukhlenko, and M. Premaratne, Spaser made of graphene and carbon nanotubes, ACS Nano. **8**, 2431 (2014).

[37] D. Li and M. I. Stockman, Electric Spaser in the Extreme Quantum Limit, Phys. Rev. Lett. **110**, 106803 (2013).

[38] D. Y. Fedyanin, Toward an electrically pumped spaser, Opt. Lett. **37**, 404 (2012).

[39] M. Ghorbanzadeh, S. Jones, M. K. Moravvej-Farshi, and R. Gordon, Improvement of sensing and trapping efficiency of double nanohole apertures via enhancing the wedge plasmon polariton modes with tapered cusps, ACS Photonics. **4**, 1108 (2017).

[40] M. Samadi, S. Vasini, S. Darbari, A. A. Khorshad, S. N. S. Reihani, and M. K. J. Moravvej-Farshi, Hexagonal arrays of gold triangles as plasmonic tweezers, Opt. Express. **27**, 14754 (2019).

[41] M. D. Fischbein and M. J. N. l. Drndic, Sub-10nm device fabrication in a transmission electron microscope, Nano Lett. **7**, 1329 (2007).

[42] X.-T. Kong, R. Zhao, Z. Wang, and A. O. J. N. l. Govorov, Mid-infrared plasmonic circular dichroism generated by graphene nanodisk assemblies, Nano Lett. **17**, 5099 (2017).

[43] J. S. Yu, S. Slivken, A. Evans, S. R. Darvish, J. Nguyen, and M. Razeghi, High-power λ∼9.5μm quantum-cascade lasers operating above room temperature in continuous-wave mode, Appl. Phys. Lett. **88**, 091113 (2006).

[44] A. Dalili, E. Samiei, and M. J. A. Hoorfar, A review of sorting, separation, and isolation of cells and microbeads for biomedical applications: Microfluidic approaches, Analyst **144**, 87 (2019).

[45] R. Paiella, *Intersubband Transitions in Quantum Structures* (The McGraw-Hill Companies, New York, 2006).

[46] M. I. Stockman, Nanoplasmonics: Past, present, and glimpse into future, Opt. Express **19**, 22029 (2011).

[47] R. Ferreira and G. Bastard, Evaluation of some scattering times for electrons in unbiased and biased single- and multiple-quantum-well structures, Phys. Rev. B **40**, 1074 (1989).

[48] J. Faist, F. Capasso, C. Sirtori, D. L. Sivco, A. L. Hutchinson, and A. Y. Cho, Vertical transition quantum cascade laser with bragg confined excited state, Appl. Phys. Lett. **66**, 538 (1995).

[49] M. Premaratne and M. I. Stockman, Theory and technology of SPASERs, Advances Optics Photonics **9**, 79 (2017).

[50] D. J. Bergman, The dielectric constant of a composite material- a problem in classical physics, Phys. Rep. **43**, 377 (1978).

[51] D. J. Bergman, Dielectric constant of a two-component granular composite: A practical scheme for calculating the pole spectrum, Phys. Rev B **19**, 2359 (1979).

[52] D. J. Bergman, The dielectric constant of a simple cubic array of identical spheres, J. Phys. C: Solid State Phys **12**, 4947 (1979).

[53] David J. Bergman, Exactly Solvable Microscopic Geometries and Rigorous Bounds for the Complex Dielectric Constant of a Two-Component Composite Material, Phys. Rev. Lett. **44**, 1285 (1980).

[54] D. J. Bergman, Bounds for the complex dielectric constant of a two-component composite material, Phys. Rev. B **23**, 3058 (1981).

[55] R. W. Cohen, G. D. Cody, M. D. Coutts, and B. Abele, Optical properties of granular silver and gold films, Phys. Rev. B **8**, 3689 (1973).

[56] L. Falkovsky and A. A. Varlamov, Space-time dispersion of graphene conductivity, Eur. Phys. J B. **56**, 281 (2007).

[57] S. Thongrattanasiri, A. Manjavacas, and F. García de Abajo, Quantum finite-size effects in graphene plasmons, ACS Nano. **6**, 1766 (2012).

[58] V. E. Babicheva, I. V. Kulkova, R. Malureanu, K. Yvind, and A. V. Lavrinenko, Plasmonic modulator based on gain-assisted metal–semiconductor–metal waveguide, Photonics Nanostructures Fundamentals Appl. **10**, 389 (2012).

[59] J. Xiao, H. Zheng, Y. Sun, and Y. X. Yao, Bipolar optical forces on dielectric and metallic nanoparticles by an evanescent wave, Opt. Lett. **35**, 962 (2010).

[60] K. Wang, E. Schonbrun, P. Steinvurzel, and K. Crozier, Scannable plasmonic trapping using a gold stripe, Nano Lett. **10**, 3506 (2010).

[61] X. Han, V. G. Troung, P. S. Thomas, and S. N. Chormaic, Sequential trapping of single nanoparticles using a gold plasmonic nanohole array, Photonics Res. **6**, 981 (2018).

[62] A. A. Saleh, S. Sheikhoelislami, S. Gastelum, and J. A. Dionne, Grating-flanked plasmonic coaxial apertures for efficient fiber optical tweezers, Opt. Express. **24**, 20593 (2016).

[63] K. Svoboda and S. M. Block, Optical trapping of metallic Rayleigh particles, Opt. Lett. **19**, 930 (1994).

[64] D. Erickson, X. Serey, Y. F. Chen, and S. Mandal, Nanomanipulation using near field photonics, Lab on Chip **11**, 995 (2011).

[65] Z. Fang, S. Thongrattanasiri, A. Schlather, Z. Liu, L. Ma, Y. Wang, P. M. Ajayan, P. Nordlander, N. J. Halas, and F. J. García de Abajo, Gated tunability and hybridization of localized plasmons in nanostructured graphene, ACS Nano **7**, 2388 (2013).

[66] B. J. Roxworthy and K. C. Toussaint, Jr., Femtosecond-Pulsed plasmonic nanotweezers, Sci. Rep. **2**, 660 (2012).

[67] Y. Tanaka, S. Kaneda, and K. Sasaki, Nanostructured potential of optical trapping using a plasmonic nanoblock pair, Nano Lett. **13**, 2146 (2013).

[68] A. Ashkin, J. M. Dziedzic, J. E. Bjorkholm, and Steven Chu, Observation of a single-beam gradient force optical trap for dielectric particles, Optics Lett. **11**, 288 (1986).